

A Robust RFI Identification For Radio Interferometry based on a Convolutional Neural Network

Haomin Sun^{1,2}, Hui Deng^{1,2*}, Feng Wang^{1,2†}, Ying Mei^{1,2}, Tingting Xu^{1,2},
Oleg Smirnov³, Linhua Deng⁴, and Shoulin Wei⁵

¹ Center For Astrophysics, Guangzhou University, Guangzhou 510006, P.R. China

² Great Bay Center, National Astronomical Data Center, Guangzhou, Guangdong, 510006, P.R. China

³ Department of Physics and Electronics, Rhodes University, PO Box 94, Makhanda 6140, South Africa

⁴ Yunnan Observatory, Chinese Academy of Sciences, Kunming, Yunnan, 650216, P.R. China

⁵ Key Lab Of Computer Technology Appliace, Kunming University of Science And Technology, Kunming, Yunnan, 650500, P.R. China

Accepted XXX. Received YYY; in original form ZZZ

ABSTRACT

The rapid development of new generation radio interferometers such as the Square Kilometer Array (SKA) has opened up unprecedented opportunities for astronomical research. However, anthropogenic Radio Frequency Interference (RFI) from communication technologies and other human activities severely affects the fidelity of observational data. It also significantly reduces the sensitivity of the telescopes. We proposed a robust Convolutional Neural Network (CNN) model to identify RFI based on machine learning methods. We overlaid RFI on the simulation data of SKA1-LOW to construct three visibility function datasets. One dataset was used for modeling, and the other two were used for validating the model’s usability. The experimental results show that the Area Under the Curve (AUC) reaches 0.93, with satisfactory accuracy and precision. We then further investigated the effectiveness of the model by identifying the RFI in the actual observational data from LOFAR and MeerKAT. The results show that the model performs well. The overall effectiveness is comparable to AOFlogger software and provides an improvement over existing methods in some instances.

Key words: methods: data analysis, techniques: interferometric, software: simulations

1 INTRODUCTION

During the past two decades, multiple radio telescopes have been commissioned or scheduled to be built. Several pathfinders of the Square Kilometer Array (SKA) (Braun 1996), i.e., the Murchison Widefield Array (MWA) (Lonsdale et al. 2009), the Australian SKA Pathfinder (ASKAP) (Macquart et al. 2010), the South African MeerKAT (Booth & Jonas 2012), and the Low Frequency Array (LOFAR) (de Vos et al. 2009), have been put into routine observation, laying the foundation for the construction of the SKA.

Any unwanted signal in radio astronomy is considered Radio Frequency Interference (RFI), regardless of whether it is intentional or not. RFI affects all radio astronomy telescopes and often originates in intentional emitters such as digital TV, mobile and satellite communications systems etc. (Offringa et al. 2015) showed that DTV, radio, and satellite communication had become significant sources of local RFI. In general, flagging the visibility function data affected by RFI is necessary for modern radio interferometers. Incorrectly

flagged visibility data causes incorrect imaging results (Perley & Cornwell 2003).

Identification and mitigation of RFI has attracted a substantial amount of research work. The basic principle is to set a threshold for the amplitude of the data to detect RFI (Parsons et al. 2014). AOFlogger, a tool for mitigating RFI used by LOFAR, adopted the SumThreshold method (Offringa et al. 2010). RFIMS method was proposed for the Westerbork Synthesis Radio Telescope is based on a powerful field-programmable gate array processor (Baan et al. 2004). The polarization information of post-correlation interference signals is used to detect and mitigate RFI (Yatawatta 2021). These methods have significantly improved the development of high-precision radio observations with outstanding results. However, SKA science goals have led to new challenges for traditional RFI identification and mitigation methods. For example, exploring Epoch of Reionization (EoR) is one of the most important scientific goals of the SKA, which requires a data reduction system to identify and mitigate faint radio frequency interference (i.e., low-level RFI) (Offringa et al. 2019).

It is worth exploring some new approaches to solve the RFI problem faced by radio interference arrays. Deep learning is

* E-mail: denghui@gzhu.edu.cn

† E-mail: fengwang@gzhu.edu.cn

being used widely and extensively for classification problems in recent years. Convolutional neural networks (CNN) are being adopted in image recognition. U-Net enables the classification of clean signal and RFI signatures in 2D time-ordered data by using a particular type of CNN (Akeret et al. 2017). R-Net algorithm and transfer learning seem to be a practical algorithm for mitigating RFI (Vafaei Sadr et al. 2020). The deep fully convolutional neural network works well by using both amplitude and phase information to identify RFI (Kerrigan et al. 2019). The algorithm for identifying RFI based on deep learning (e.g., U-Net) often requires a large amount of RFI data to train the neural network, and its accuracy also depends on whether a correct label map is given to the neural network (Vafaei Sadr et al. 2020).

Our research focused on the application of CNN on RFI identification. We studied RFI simulation methods, constructed a CNN model for the visibility functions simulated from the SKA1-LOW configuration, and applied the model to the real observational data from two radio telescopes. The rest of this study is organized as follows.

Sec. 2 constructs a CNN model for the RFI identification. Sec. 3 describes the simulation process, including visibility data simulation and RFI simulation, checks out CNN model on the simulated data based on the configuration of SKA1-LOW. Sec. 4, applies our model to the real observational data from MeerKAT and LOFAR. Sec. 5 evaluates our CNN model and discusses some issues. Sec. 6 gives conclusions.

2 METHOD

2.1 Data

The radio interferometer reconstructs spatial and spectral information from incomplete visibilities sampled at multiple observational frequencies. An interferometric array provides samples of the complex visibility functions of the sources in the (u, v) plane (Cornwell et al. 1999). The visibility function $V(u, v)$ is related to the source intensity distribution $I(l, m)$ (multiplied by the primary beam of the array elements) by a two-dimensional Fourier transform:

$$V(u, v) = \iint_S I(l, m) e^{-2\pi i(ul+vm)} dl dm \quad (1)$$

where l and m are east-west, and north-south angles on the sky, u and v are east-west and north-south spatial frequencies.

From the visibility data, there is a difference between the astronomical signal affected by RFI and the normal astronomical signal (Baan 2011). Fig. 1 shows the amplitude and phase of the visibility data for time vs. frequency. It is evident find that the data without RFI contains stable values in amplitude and phase, while the RFI-Polluted data contains values that change significantly.

When using CNN patterns to identify and mitigate RFI, we must first construct the underlying dataset so that the CNN can learn features that exist in the amplitude and phase information of the visibility data, then transform the identification of RFIs into a binary classification. We took the amplitude and phase values to form a data pair, and all the data pairs constituted the dataset for the following CNN modeling.

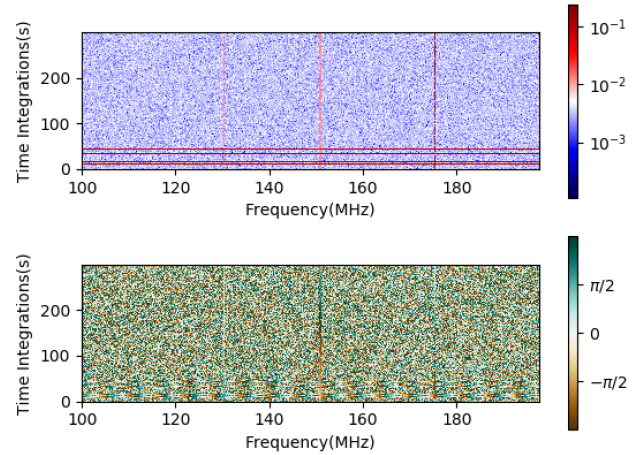


Figure 1. An example of SKA1-LOW visibility simulated from baseline SKA1-LOW020 - SKA1-LOW004. The top panel shows the amplitude. The bottom panel shows the phase. The two maps provide some information about the RFI, which has constant narrow-band RFI in the channel of 130MHz, 152MHz, and 178MHz, and broad-band RFI happens from 10 to 40 seconds.

2.2 CNN Design

We proposed a dichotomous model to identify RFI after analyzing the data features with RFI. The model is inspired by a classic architecture named Le-Net architecture (LeCun et al. 1998), which has a good performance in many domains such as image classification (El-Sawy et al. 2016), pattern recognition (Yuan et al. 2012) and computer vision (Xie et al. 2016).

The model consists of 4 convolutional layers, 4 Max-pooling layers, and 2 fully connected layers. For the first two convolutional layers, we chose a convolutional kernel of 1×2 and used one as the parameter for striding and padding. The remaining convolutional layers have a convolutional kernel size of 3×3 . The parameters of striding and padding are the same as that of the first two convolutional layers. For each convolutional layer, we chose Batch Normalization (BN) (Ioffe & Szegedy 2015) as regularization to speed up the training rate of the model. We chose Rectified Linear Unit (ReLU) (Nair & Hinton 2010) which is the most popular activation function for the activation layer which can generate a non-linear mapping between the input and output. We added a max-pooling layer after each of the other convolutional layers, excluding the first convolutional layer. In the max-pooling layer, the kernel size of the first two layers are 1×2 , and the kernel sizes of the last two layers are 2×2 and 3×3 , respectively.

After the features were obtained through convolutional processing, we added fully connected layers to map the learned "distributed feature representation" to the sample labeling space. For our first fully connected layer, we chose Dropout (Hashemi 2012) as regularization to prevent overfitting and ReLU as the activation function. The final classification results were output by the classifier softmax in the last fully connected layer. The network is shown in Fig. 2, and the detailed information is listed in Table 1.

The model has been extensively tested and optimized and is the best of all model networks in the study. We initially

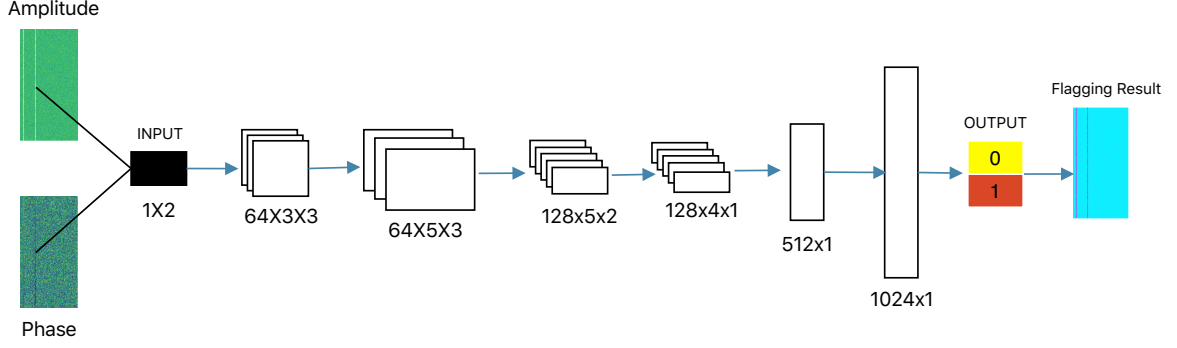


Figure 2. Schematic diagram of the CNN model architecture.

Table 1. Architecture overview of the CNN model proposed in the study.

| Layer | Type | Channels | Kernel Size | Striding | Padding | Regularization | Activation |
|-------|--------------|----------|-------------|----------|---------|----------------|------------|
| IN | INPUT | 1 | 1×2 | 1 | 1 | BN | ReLU |
| C2 | Convolution | 64 | 1×2 | 1 | 1 | BN | ReLU |
| M3 | Max Pooling | 64 | 1×2 | 1 | 0 | ... | ... |
| C4 | Convolution | 64 | 3×3 | 1 | 1 | BN | ReLU |
| M5 | Max Pooling | 64 | 1×2 | 1 | 0 | ... | ... |
| C6 | Convolution | 128 | 3×3 | 1 | 1 | BN | ReLU |
| M7 | Max Pooling | 128 | 2×2 | 1 | 0 | ... | ... |
| C8 | Convolution | 512 | 3×3 | 1 | 1 | BN | ReLU |
| M9 | Max Pooling | 512 | 3×3 | 2 | 0 | ... | ... |
| FL10 | FlattenLayer | 512 | ... | ... | ... | Dropout | ReLU |
| OUT | FlattenLayer | 1024 | ... | ... | ... | ... | Softmax |

used convolution kernels of 1×1 and 1×2 to build the network. However, it was eventually found that the feature map had to be extended using the padding method to effectively extract the input data (1×2) features.

The number of layers and normalizations of the model are obtained after many trials. The trial results show that the detection efficiency of RFI with a four-layer network is optimal to maximize the learning time and minimize the prediction time and enable the network to learn as much as possible the abstract features of RFI. The hyperparameters are also guided by the test results obtained from extensive trials.

2.3 Model training and testing

For a given dataset, we set the batch size as 16 and iteration time as 100, selected 16 samples each time to train the model. In the end, We selected the best performance model.

Each training sample was given a prediction label after training, and the loss was obtained by feeding the prediction label and true label into the loss function. We updated the parameters of the model by backpropagation to obtain the minimum loss. We used the gradient descent algorithm to update the parameters. The final loss value converged to some constant values through iterative training. We chose

the SGD (Stochastic Gradient Descent) (Montavon et al. 2012) method for the momentum update and set the SGD parameters to the specified values, where the learning rate was 0.001 (Wilson & Martinez 2003), and the momentum was 0.9 (Sutskever et al. 2013). Both of these values are standard values obtained from a large number of previous experiments in the field of deep learning.

After training, we used a test set to test the model and calculated evaluation metrics of the model.

2.4 Model Evaluation

Recall, Accuracy, and Precision are used to evaluate the results of the Le-Net. The three metrics are defined as follows:

$$\text{Recall} = \frac{\text{TP}}{\text{TP} + \text{FN}} \quad (2)$$

$$\text{Precision} = \frac{\text{TP}}{\text{TP} + \text{FP}} \quad (3)$$

$$\text{Accuracy} = \frac{\text{TP} + \text{TN}}{\text{TP} + \text{FN} + \text{FP} + \text{TN}} \quad (4)$$

where TP , TN , FP , FN represent True Positive, True Negative, False Positive, and False Negative, respectively.

It is important to note that the number of each type of dataset was unbalanced, which would result in a decrease of the performance of the Le-Net model (Bhowan et al. 2012). Therefore, we plotted the ROC (Receiver Operating Characteristic) curve, computed the AUC (Area Under roc Curve) (Bradley 1997) value and took AUC as a metric to evaluate our CNN model.

3 SKA1-LOW RFI MITIGATION

SKA1-LOW (Mellema et al. 2013) is the low-frequency (50-350 MHz) telescope of the SKA Phase 1, to be constructed in Western Australia. There are 512 stations distributed mainly within a dense area around the center of the SKA1-LOW, and each station consists of 256 log-periodic dual-polarized antennas. It will be used to study the early epochs of the universe by looking at the red shifted signal from the 21 cm Hydrogen emission line. The reason for using the SKA1-LOW instead of the SKA1-MID for the research of the RFI mitigation is that the low-frequency interferometer is more susceptible to interference from RFI signals and presents more difficulties for RFI mitigation. This is due to the low-frequency bands being heavily in use by many communication systems. That results in strong signals all over the bands (Baan 2011).

3.1 SKA1-LOW Data Preparation

3.1.1 Visibility Data Simulation

We developed a simulation software for the study based on the SKA Radio Astronomy Simulation, Calibration and Imaging Library (RASCIL)¹ that expresses radio interferometry calibration and imaging algorithms in Python and NumPy. The SKA SIM/ORCA agile team has developed a series of software for SKA1-LOW and SKA1-MID, verifying RASCIL's accuracy and robustness.

We simulated observations of the SKA1-LOW telescope based on the telescope configurations given in the SKA design baseline document (Dewdney et al. 2019). The flow chart of the simulation is shown in Fig. 3. At the same time, we used the Extragalactic All-sky MWA (GLEAM) catalog (Wayth et al. 2015) to simulate the observation of point sources because the MWA telescope is one of the pathfinders for the SKA and its observational band and location are similar to that of SKA1-LOW. The Gleam survey contains 307,455 radio sources with 20 separate flux density measurements across 72 - 231 MHz (Wayth et al. 2015).

We generated three datasets with different periods. We simulated observations for 1000 channels ranging from 100 MHz to 200 MHz. The observation time is 10 minutes. The bandwidth of each channel is 0.1MHz. We only generated the visibility functions of Stokes I and stored the results in a Numpy array with a shape of (300,31,31,1000,1) that corresponds to (Time, Antenna1, Antenna2, Frequency, Polarization). Ultimately, we stored the three datasets in

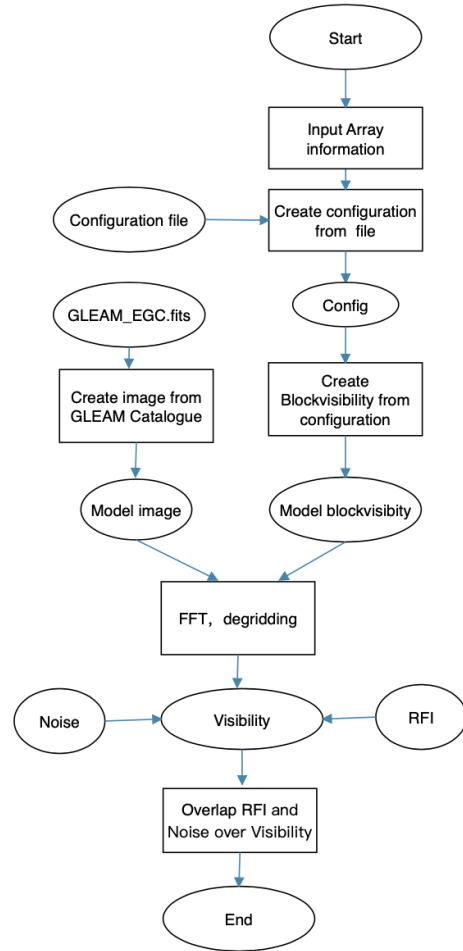


Figure 3. The flow chart for SKA1-LOW simulation observation

three Measurement Sets, i.e., Sim_RFI-1, Sim_RFI-2, and Sim_RFI-3, respectively.

3.1.2 RFI Simulation

We adapted the hera_sim² package and applied it to the RFI simulation. The hera_sim package has already made a significant contribution to the simulation of RFI (Kerrigan et al. 2019). Both HERA and SKA1-LOW regard the detection of EOR as their important scientific goal and focus on the research of the frequency scope from 100 - 200 MHz where EOR is likely to be detected (de Lera Acedo et al. 2018; Thyagarajan 2017).

We considered narrowband RFI and broadband RFI in the RFI simulation. The narrowband RFI is the primary RFI commonly caused by DTV, satellite communications, commercial FM. The broadband RFI is transient and strong, usually from the lightning and transmission cables. We added the two types of RFI with different ratios to the visibility data obtained in Section 3.1.1 and generated three RFI-polluted measurement set (MS) files named Sim_RFI-1, Sim_RFI-2, and Sim_RFI-3, respectively. The visibility functions of the three new MS files are stored in three Numpy arrays with

¹ <https://gitlab.com/ska-telescope/external/rascil>

² https://github.com/HERA-Team/hera_sim

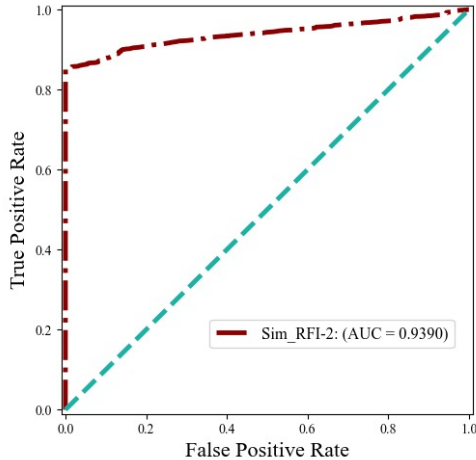


Figure 4. The ROC curve for training Sim_RFI-2 data. The value of AUC is 0.9390.

the same shape as the original MS files. The details of these RFI-polluted files are given in Table 2.

3.2 Dataset

Each MS file generated in Section 3.1.1 and Section 3.1.2 is 1.25GB in size. Hence the total size of the six MS files reaches 7.5GB. We selected the visibility data from the baseline SKA1-LOW020 to SKA1-LOW004. Each MS file has 300000 data pairs (amplitude, phase). Hence, the total number of data pairs we used are 300000×6 .

We randomly selected 80% data pairs from the Sim_RFI-2 as the training set and the left 20% as the testing set. The visibility data from the other two RFI-polluted MS files (i.e., the Sim_RFI-1 and the Sim_RFI-3) and the three original MS files are used to test the robustness of the model. Since the SKA1-LOW data are all simulated and generated, labeling the data is trivial.

3.3 CNN Modelling

Through training with the data of Sim_RFI-2, we obtained a CNN model with the recall of 97.2%, the precision of 99.1%, and the accuracy of 99.8%. The ROC curves are shown in Fig. 4.

3.4 Results

We fed the two simulated RFI-polluted validation sets (Sim_RFI-1 and Sim_RFI-3) into the trained CNN model. The flagging results of our CNN model and AOflagger are presented in Fig. 5. The performance evaluation is given in Table 3. Since the thresholding based on the three-sigma rule (Pukelsheim 1994) is often used in traditional data processing to identify outliers of data, we also added the flagging results under different thresholds for comparison.

We also applied our CNN model and AOflagger to identify RFI in the dataset without RFI, i.e., the datasets of Sim-1, Sim-2, and Sim-3. The result shows that our CNN model

detected no false-positive RFI. The average false-positive RFI ratio of AOflagger was 0.13%. (Offringa et al. 2013) estimated that misdetection of AOflagger accounts for approximately 0.4% of detections. Therefore, we think 0.13% should be the misidentification of AOflagger.

4 RFI MITIGATION FOR DATA FROM LOFAR AND MEERKAT

We further applied our model to real observational data from LOFAR and MeerKAT.

4.1 RFI mitigation for data from LOFAR

LOFAR is a new-generation radio interferometer constructed in the north of the Netherlands and across Europe. Utilizing a novel phased array design, LOFAR covers the frequency range of 10 to 240 MHz and provides unique observing capabilities. We used its 10 minutes of visibility data, named as LOFAR-Set, for the following research. LOFAR-Set consists of 64 channels covering from 137.21MHz to 137.39MHz. Fig. 6 shows the information of the amplitude and phase, in which RFI is easy to be found. We used the first 200 seconds, i.e., 12800 data pairs (amplitude, phase), for testing, and the other 400 seconds, i.e., 25600 data pairs (amplitude, phase), for training.

Although the RFI in Fig. 6 is obvious, it is not marked or flagged. In others words, the dataset of LOFAR-Set is not labeled for CNN. Therefore, we used AOflagger with its default SumThreshold to flag the training dataset of the LOFAR-Set and took the flagging results as the reference truth. From the experimental results in Sec.3, AOflagger cannot fully identify the RFI. Therefore, the labels flagged by AOflagger are not the ground truth but are still an essential reference for us.

The flagging results are shown in Fig. 7.

4.2 RFI mitigation for data from Meerkat

The MeerKAT radio telescope is a precursor of the SKA mid-frequency telescope, located in the arid Karoo region of the Northern Cape Province in South Africa. It comprises 64 antennas with a diameter of 13.5 meters. The observational data from MeerKAT we used, named MeerKAT-Set here, consists of a calibrator scan and a target scan, with a frequency band from 857.15MHz to 1.71GHz. The calibrator was scanned for 10 minutes, 4096 channels, so the number of data pairs is 303030. The target was scanned for 15 minutes, 1024 channels, so the number of data pairs is 114688. The 303030 data pairs are used for training, and the 114688 data pairs are used for testing. The top row in Fig. 8 is the map of the amplitude values of the target observation.

Like the dataset of LOFAR-Set, the dataset of MeerKAT-Set is not labeled either. We used AOflagger with default SumThreshold to flag the training dataset of MeerKAT-Set and set the results as the ground truth. In addition, MeerKAT commonly uses "Tricolour" for flagging³. Tricolour is a specified AOflagger version that can be run under the

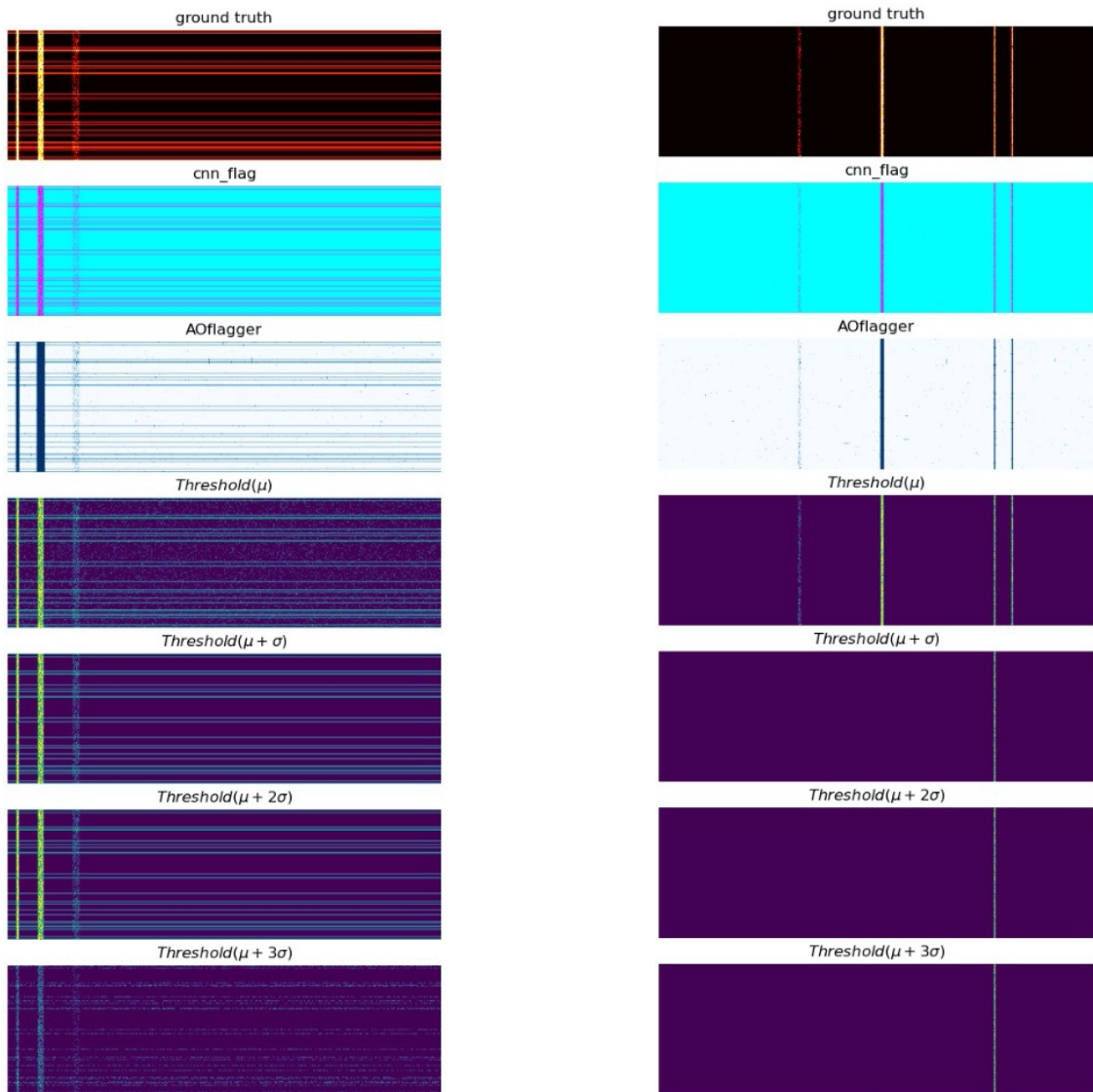
³ <https://github.com/ska-sa/tricolour>

Table 2. The information of the RFI-polluted data. Amp represents the amplitude of the RFI, the μ and σ represent the mean and standard deviation of the overall data.

| Data set | Sim_RFI-1 | Sim_RFI-2 | Sim_RFI-3 |
|------------------------------|--|---------------------------------------|-------------------------------------|
| Phase-centre | RA=+15°, Dec=-45° | RA=+30°, Dec=-45° | RA=+45°, Dec=-45° |
| Observation time(2020-01-01) | 10:27 - 10:37 | 11:27 - 11:37 | 12:23 - 12:33 |
| RFI ratio | 10% | 7.5% | 1.1% |
| RFI composition | 70%Narrow band RFI + 30%Broad band RFI | 90%Narrow band RFI+ 10%Broad band RFI | 100%Narrow band RFI |
| RFI strength | $\mu < \text{Amp} < \mu + 13\sigma$ | $\mu < \text{Amp} < \mu + 15\sigma$ | $\mu < \text{Amp} < \mu + 15\sigma$ |

Table 3. Performance evaluation of CNN and AOflagger on the RFI-polluted validation data sets.

| Data Set | CNN | | | AOflagger | | |
|-----------|--------|-----------|----------|-----------|-----------|----------|
| | Recall | Precision | Accuracy | Recall | Precision | Accuracy |
| Sim_RFI-1 | 97.4% | 97.5% | 97.8% | 100% | 88.2% | 98.7% |
| Sim_RFI-3 | 99.7% | 99.4% | 99.8% | 99.8% | 71.9% | 97.1% |

**Figure 5.** Flagging results of Sim_RFI-1 (left) and Sim_RFI-3 (right) with different methods. In each panel, the horizontal axis is frequency, and the vertical axis is time.

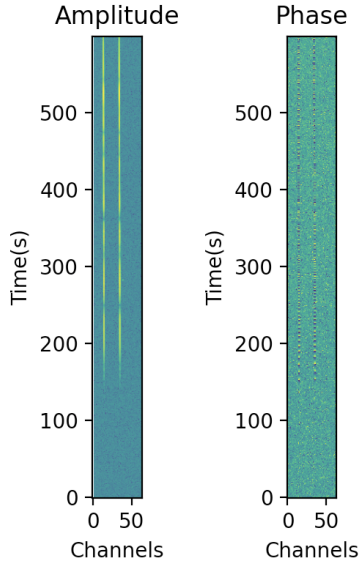


Figure 6. The visibility data of LOFAR-Set. The left row shows the amplitude value and the right row shows the phase value. The data pairs of the first 200 seconds are used for testing, and the left 400 seconds used for training.

Dask framework (Dask Development Team (2016)). Tricolour uses a severe strategy for calibrator scan. We also used Tricolour to flag the training dataset of MeerKAT-Set and set the result as the ground truth.

The flagging results are shown in Fig. 8.

5 DISCUSSION

5.1 Generalisation

Due to the relatively small number of data samples, the ability to generalise the model cannot be verified very accurately yet. The model obtained by training the simulated dataset Sim_RFI-2 shows satisfactory RFI identification on Sim_RFI-1 and Sim_RFI-3. In addition, the model adapts well to real observed datasets from LOFAR and MeerKat. The current proposed CNN model has a certain generalization ability from these results, but more data are needed to test it.

5.2 Comparison with AOFlagger

AOFlagger uses a morphology-based RFI detection algorithm. It is more sensitive to changes in the data between adjacent channels, which easily allows AOFlagger to identify as much RFI-contaminated data as possible.

Table 3 shows that for the simulated datasets, the accuracy of our CNN model and AOFlagger is almost the same. However, the precision of our model is higher than AOFlagger. By contrast, the recall of AOFlagger is slightly higher. The possible reason is that we fed the training data into the CNN model for training in an unordered manner, which aligns with the feature that the time RFI happens has nothing to do with frequency. It is equivalent to reducing the redundancy of irrelevant features.

Fig. 9 is a partial zoomed-in diagram of the Sim_RFI-3

Table 4. The running time comparison of CNN and AOflagger. Both of them use an Intel(R) Xeon(R) CPU E5-2620 v4 @ 2.10GHz.

| Data set | Time(CNN) | Time(AOflagger) |
|-------------|-----------|-----------------|
| Sim_RFI-1 | 31s | 18s |
| Sim_RFI-2 | 31s | 17s |
| Sim_RFI-3 | 32s | 18s |
| LOFAR-Set | 4s | 1s |
| MeerKAT-Set | 142s | 98s |

data set. It is evident that AOFlagger uses morphology to identify, as illustrated by the misidentification of the edges as RFI. Our proposed CNN-based recognition method can correctly identify the visibilities at the edges and can obtain a more reliable identification than AOFlagger.

5.3 Weak RFI detection

For some traditional RFI detection algorithms based on the changes of the adjacent signal, the intensity is one of the essential criteria for detection. Therefore, we also consider RFI with different intensities in our experiments.

We make a comparison of the traditional threshold method and our CNN model. The result (See Fig. 5) shows that there exists some difference between the two methods. Since the intensity of RFI is uncertain, RFI cannot be well identified by setting a definite threshold value. Our CNN model performs better on flagging different intensities of RFI on the simulation data (which has ground truth) than the threshold method, which indicates a potential advantage for weak RFI detection.

5.4 RFI Identification Speed

The speed of the proposed CNN-based RFI identification is slower than AOflagger. We compared the running time between our CNN model and AOflagger. The result in Table 4 shows that AOflagger is nearly twice as fast as our CNN model except for the LOFAR-Set. The speed of AOflagger for LOFAR-Set is four times as fast as our model. Therefore, AOFlagger is suitable for real-time processing, and the detection method of CNN models is suitable for subsequent scientific studies.

5.5 Limitations

The CNN model obtained by training a part of the LOFAR-Set (200-600s) has partially different labeling results from AOflagger when identifying RFI in other parts of the LOFAR-Set. The possible reason is that we only used the default RFI tagging strategy of AOflagger.

The computational cost of our CNN model is unsatisfactory as per Table 4. The possible reason is that our CNN model is built on Python-based PyTorch framework (Paszke et al. 2019). Le-Net does not have a speed advantage over AOflagger, for the latter is based on C++ language. Much work for optimizing our implementation remains to be done.

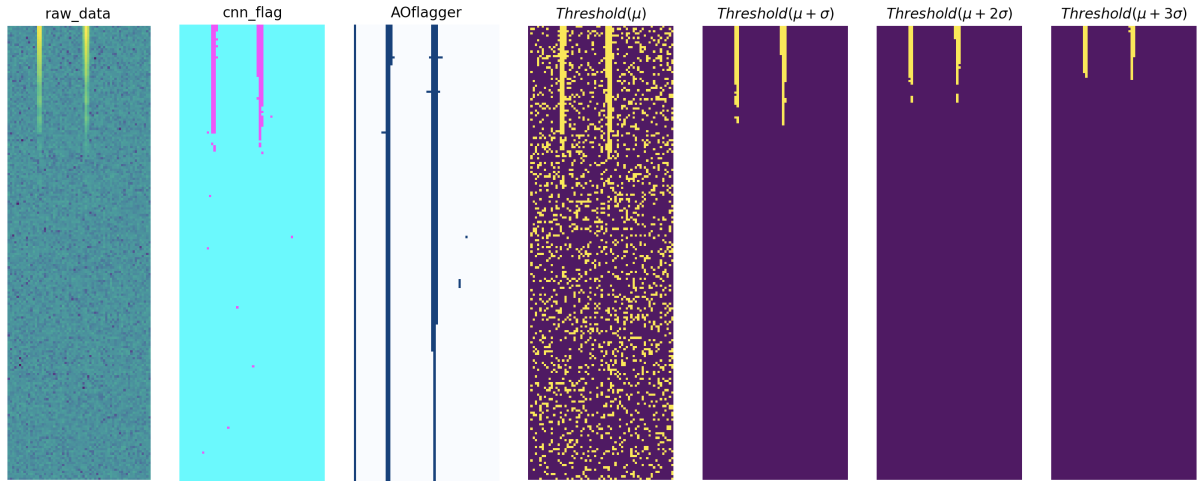


Figure 7. The results of the different RFI mitigation methods for LOFAR-Set. The horizontal axis is frequency, and the vertical axis is time. The first row is the amplitude of the testing data. The second and the third row are flagging results of our CNN method and the AOflagger, respectively. The others correspond to applying different thresholds to the data for flagging.

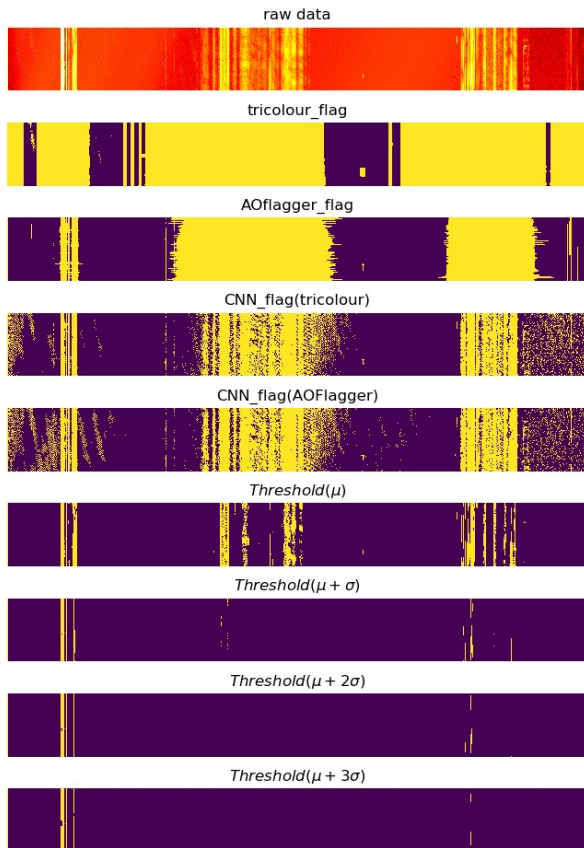


Figure 8. The results of the different RFI mitigation methods for MeerKAT-Set. The horizontal axis represents channels, and the vertical axis represents time. The first row shows the testing data, i.e., the target scan. The second and third rows are the flagging results of Tricolour and AOflagger, respectively. The fourth and fifth rows show the flagging results of our CNN model with the ground truth obtained from Tricolour and AOflagger, respectively.

6 CONCLUSION

RFI identification is an indispensable work for the data processing of next generation radio telescopes. This paper describes a method for simulating observations of SKA1-LOW by RASCIL and hera_sim package to obtain reliable simulation data, designs a CNN model and applies it to the simulated data and the real data from Meerkat and LOFAR. The results show that our CNN model has a good performance in RFI identification.

However, we realize that there are still some limitations with our CNN model. First, we need real ground truth to guide the training data to a well-performing model. Currently, we have to manually review the correctness of the flags used for the training data. Second, the Python-based LeNet has limitations in its computational speed, which makes its efficiency unsatisfactory.

The random nature of the human activity and the geographical variability of telescopes make identifying RFI a difficult task. At the same time, weak signals such as the cosmic microwave background and EoR also place high demands on the accuracy of RFI identification. In future work, we will continue to refine the method for SKA1-LOW observation simulations and try to use GPU for our model or use parallel computing to boost the computing speed of our CNN model. We will also try to use reference antennas to get a more accurate ground truth to enhance the ability of our model to identify RFI.

ACKNOWLEDGEMENTS

This work is supported by the National SKA Program of China (2020SKA0110300), the Joint Research Fund in Astronomy (U1931141,U1831204) under cooperative agreement between the National Natural Science Foundation of China (NSFC) and the Chinese Academy of Sciences (CAS), the Funds for International Cooperation and Exchange of the National Natural Science Foundation

of China (11961141001), the National Natural Science Foundation of China (No.11903009), the Innovation Research for the Postgraduates of Guangzhou University (2020GDJC-D20), Fundamental and Application Research Project of Guangzhou (202102020677)

This work is also supported by Astronomical Big Data Joint Research Center, co-founded by National Astronomical Observatories, Chinese Academy of Sciences and Alibaba Cloud. In addition, many thanks to all the members of the RASCIL development team.

We do appreciate the anonymous referee for valuable and helpful comments and suggestions.

7 DATA AVAILABILITY

All the program code and part of the test data are stored in Github repository, the link is https://github.com/astronomical-data-processing/CNN_RFI.git.

REFERENCES

- Akeret J., Chang C., Lucchi A., Refregier A., 2017, *Astronomy and computing*, 18, 35
- Baan W. A., 2011, in 2011 XXXth URSI General Assembly and Scientific Symposium. pp 1–2
- Baan W. A., Fridman P., Millenaar R., 2004, *The Astronomical Journal*, 128, 933
- Bhowan U., Johnston M., Zhang M., Yao X., 2012, *IEEE Transactions on Evolutionary Computation*, 17, 368
- Booth R., Jonas J., 2012, *African Skies*, 16, 101
- Bradley A. P., 1997, *Pattern recognition*, 30, 1145
- Braun R., 1996, in Raimond E., Genee R., eds, *Astrophysics and Space Science Library Vol. 208, The Westerbork Observatory, Continuing Adventure in*. p. 167 ([arXiv:astro-ph/9512060](https://arxiv.org/abs/astro-ph/9512060)), [doi:10.1007/978-94-009-1734-7_9](https://doi.org/10.1007/978-94-009-1734-7_9)
- Cornwell T., Braun R., Briggs D. S., 1999, in *Synthesis Imaging in Radio Astronomy II*. p. 151
- Dask Development Team 2016, Dask: Library for dynamic task scheduling. <https://dask.org>
- Dewdney P., et al., 2019, Technical report, SKA1 Design Baseline Description. SKA-TEL-SKO-0001075, internal SKA document
- El-Sawy A., Hazem E.-B., Loey M., 2016, in *International conference on advanced intelligent systems and informatics*. pp 566–575
- Hashemi H., 2012, *IEEE Signal Processing Magazine*, 29, 82
- Ioffe S., Szegedy C., 2015, *CoRR*, abs/1502.03167
- Kerrigan J., et al., 2019, *Monthly Notices of the Royal Astronomical Society*, 488, 2605
- LeCun Y., Bottou L., Bengio Y., Haffner P., 1998, *Proceedings of the IEEE*, 86, 2278
- Lonsdale C. J., et al., 2009, *Proceedings of the IEEE*, 97, 1497
- Macquart J.-P., et al., 2010, *Publications of the Astronomical Society of Australia*, 27, 272
- Mellema G., et al., 2013, *Experimental Astronomy*, 36, 235
- Montavon G., Orr G. B., Müller K., 2012, 10.1007/978-3-642-35289-8, 9
- Nair V., Hinton G. E., 2010, in *Proceedings of the 27th International Conference on International Conference on Machine Learning. ICML'10*. Omnipress, Madison, WI, USA, p. 807–814
- Offringa A., de Bruyn A., Zaroubi S., Biehl M., 2010, *arXiv preprint arXiv:1007.2089*
- Offringa A., et al., 2013, *Astronomy & astrophysics*, 549, A11
- Offringa A., et al., 2015, *Publications of the Astronomical Society of Australia*, 32
- Offringa A., Mertens F., Koopmans L., 2019, *Monthly Notices of the Royal Astronomical Society*, 484, 2866
- Parsons A. R., et al., 2014, *The Astrophysical Journal*, 788, 106
- Paszke A., et al., 2019, *Advances in neural information processing systems*, 32, 8026
- Perley R., Cornwell T., 2003
- Pukelsheim F., 1994, *The American Statistician*, 48, 88
- Sutskever I., Martens J., Dahl G., Hinton G., 2013, in *International conference on machine learning*. pp 1139–1147
- Thyagarajan N., 2017, *Proceedings of the International Astronomical Union*, 12, 102
- Vafaei Sadr A., Bassett B. A., Oozeer N., Fantaye Y., Finlay C., 2020, *Monthly Notices of the Royal Astronomical Society*, 499, 379
- Wayth R., et al., 2015, *Publications of the Astronomical Society of Australia*, 32
- Wilson D. R., Martinez T. R., 2003, *Neural networks*, 16, 1429
- Xie L., Wang J., Wei Z., Wang M., Tian Q., 2016, in *Proceedings of the IEEE Conference on Computer Vision and Pattern Recognition*. pp 4753–4762
- Yatawatta S., 2021, in 2020 28th European Signal Processing Conference (EUSIPCO). pp 1961–1965

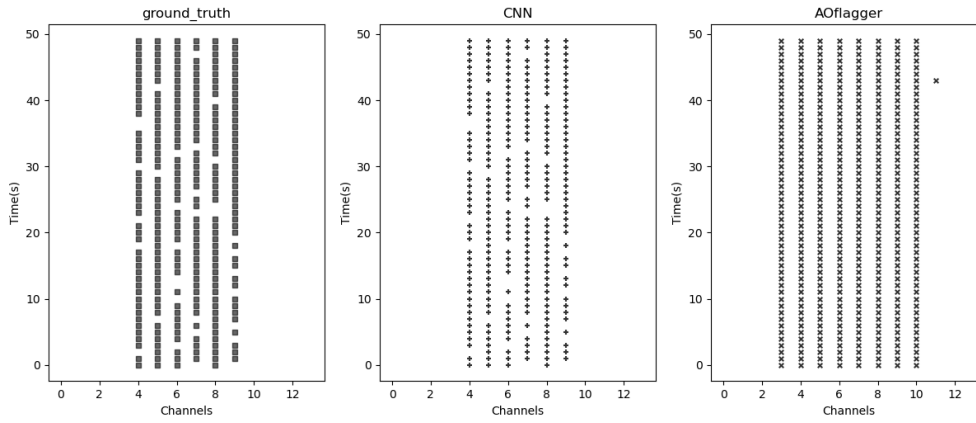


Figure 9. Zoomed-in diagram of Sim_RFI-3 data set. AOflogger incorrectly identifies the visibilities of both left and right edges.

- Yuan A., Bai G., Jiao L., Liu Y., 2012, in 2012 10th IAPR International Workshop on Document Analysis Systems. pp 125–129
- de Lera Acedo E., Pienaar H., Fagnoni N., 2018, in 2018 International Conference on Electromagnetics in Advanced Applications (ICEAA). pp 636–639
- de Vos M., Gunst A. W., Nijboer R., 2009, Proceedings of the IEEE, 97, 1431

This paper has been typeset from a $\text{\TeX}/\text{\LaTeX}$ file prepared by the author.